

Aerodynamic characteristics of 8% Scale Semi-span High-Lift Common Research Model at the JAXA 6.5m x 5.5m Low Speed Wind Tunnel

Masataka Kohzai[1], Mitsuhiro Murayama[1], Andrea Sansica[1], David Lusher[1], Takehisa Takaishi[1], & Hiroyuki Abe [1]

[1]Japan Aerospace Exploration Agency, Aviation Technology Directorate, Chofu, Tokyo, 182-8522, Japan

Abstract

JAXA participates in the international “CRM-HL Ecosystem” with the aim of supporting the validation of CFD technologies for high-lift configurations. An 8%-scale semi-span model of the NASA High-Lift Common Research Model (CRM-HL) was designed and manufactured for wind tunnel testing. Three series of wind tunnel tests were conducted in 2025 and 2026 in JAXA’s 6.5 m × 5.5 m low-speed wind tunnel to obtain baseline aerodynamic characteristics and to investigate aerodynamic and aeroacoustic phenomena associated with high-lift configurations. The test campaigns included measurements of aerodynamic force and moment coefficients, surface pressure distributions, unsteady pressure, flow visualization using surface tufts, and aeroacoustic data. In April 2025, wind tunnel tests were performed to obtain the basic performance of the CRM-HL model and to investigate the noise reduction effect of the high-lift device and main landing gear. A dedicated test conducted in November 2025 focused on stall and post-stall phenomena and included oil-flow visualization and particle image velocimetry (PIV). A further test campaign carried out from February to March 2026 primarily focused on aeroacoustic measurements, with accompanying aerodynamic measurements conducted to support the interpretation of the noise data. This paper reports the aerodynamic characteristics of the baseline CRM-HL configuration obtained from these wind tunnel experiments, with particular emphasis on the aerodynamic behavior near stall.

Keywords: CRM-HL, Wind tunnel, High-Lift Aerodynamics, CFD, validation

1. Introduction

Aerodynamic phenomena that occur near the boundaries of the flight envelope, such as buffeting and flutter, are difficult to accurately predict because they involve complex flow physics and strong multidisciplinary coupling. One of the most important regions of the boundaries is related to takeoff and landing using high-lift devices at low subsonic speeds. Lift is increased by deploying devices such as slats and flaps. Wind tunnel testing and computational fluid dynamics (CFD) are applied early in the aircraft process to develop high-lift systems and to support aerodynamic and structural evaluations. Aerodynamic flows in high-lift configurations are particularly complex due to the interaction of multiple unsteady flow phenomena, including turbulent boundary layers, vortices, and wakes, with the geometrically complex low-speed flight configurations. These characteristics make accurate CFD predictions difficult. It is important that CFD used in this region is properly validated and has a high level of reliability.

To support the validation and development of CFD technologies for high-lift configurations, NASA and Boeing defined a standardized model for takeoff and landing conditions. This model was designed to accurately represent modern passenger1 aircraft configurations and led to the establishment of the CRM‐HL Ecosystem, which consists of research institutes and aircraft manufacturers from around the world [1, 2]. An international community whose purpose is to verify the development of CFD technology for the aerodynamic analysis, design, and certification of high-lift configurations. Plans are underway to test the CRM-HL in wind tunnels at different research

institutes around the world, and to collect and share wind tunnel test data in parallel with CFD workshops, with JAXA also participating [3]. As well as having a large low-speed wind tunnel, JAXA was invited to join the CRM-HL ecosystem because it previously carried out an experimental campaign on a CRM model for cruise configuration and published the corresponding test data [4, 5]. The plan was for major wind tunnels around the world to participate in building a CRM-HL model and conducting wind tunnel tests, so it was assumed that this would become the standard model for low-speed ranges. JAXA participated in CRM-HL Ecosystem activities and began considering introducing the CRM-HL model as a standard model. The airframe noise reduction concept developed in FQUROH-2 project (Flight Demonstration of Quiet technology to Reduce Noise from High-lift Configuration) was approved to be applied not only to the project-specific aircraft undergoing flight demonstration, but also to a globally recognized general aircraft configuration, and to publish the results as a benchmark. Therefore, a CRM-HL 8% semi-span wind tunnel model was fabricated between Oct. 2023 and Feb. 2025.

The objective of the FQUROH-2 project is to demonstrate the effectiveness of the noise-reduction design concept for high-lift devices on a common configuration. We plan to publish noise source measurement data without noise reduction devices to the CRM-HL ecosystem and compare them with those obtained by NASA LaRC using a 10% CRM-HL semi-span model in the 14-by-22-foot low-speed wind tunnel. In addition, detailed aerodynamic data around the stall region of the high-lift configuration will be used for validation of the numerical tools developed as part of the Off-Design Aerodynamic Prediction Technology framework at JAXA. Through detailed comparisons between data obtained from the CRM-HL ecosystem at high Reynolds numbers and those available from JAXA low-speed wind tunnel, we will clarify Reynolds number effects. In addition to aerodynamic forces and pressure distribution data, we also plan to contribute to the CRM-HL ecosystem by providing PIV and PSP data. JAXA low-speed wind tunnel aims to improve the value of the wind tunnel by acquiring and publishing standard model data, and to improve testing techniques for high-lift configurations by exchanging information with other wind tunnels.

This paper introduces JAXA large-scale low-speed wind tunnel and provides an overview of the fabricated CRM-HL model. Two wind tunnel test series were conducted to demonstrate the effectiveness of the noise reduction design concept for high-lift devices, and one test series focused on investigating aerodynamic phenomena near stall. The present paper discusses the aerodynamic characteristics of the basic configuration and the aerodynamic behavior in the stall region. Results related to high-lift device noise reduction in the FQUROH-2 project are reported in Refs. [6–8], and noise reduction effects of the main landing gear are presented in Refs. [9–11].

2. Facility Description

The wind tunnel tests were conducted in the JAXA 6.5m x 5.5m low speed wind tunnel (JAXA LWT1), which is an atmospheric pressure closed-circuit facility. A schematic of the wind tunnel is shown in Figure 1, and its specifications are summarized in Table 1. The wind tunnel was constructed in 1965. The test section is 6.5m high, 5.5m wide, has an octagonal cross section with 1m chamfered corners, and is 9.25m long. The contraction ratio is 1/5.33, and the maximum velocity at the test section is approximately 70m/s.

The test section cart can be selected from a strut cart, which supports the model from below using struts, or a sting cart, which supports the model from behind using sting. The test section can also be used openly without a cart. For this wind tunnel test, the strut cart without the model support and equipped with a turntable was used. The angle of attack (AoA) can be set using the rotation of the turntable.

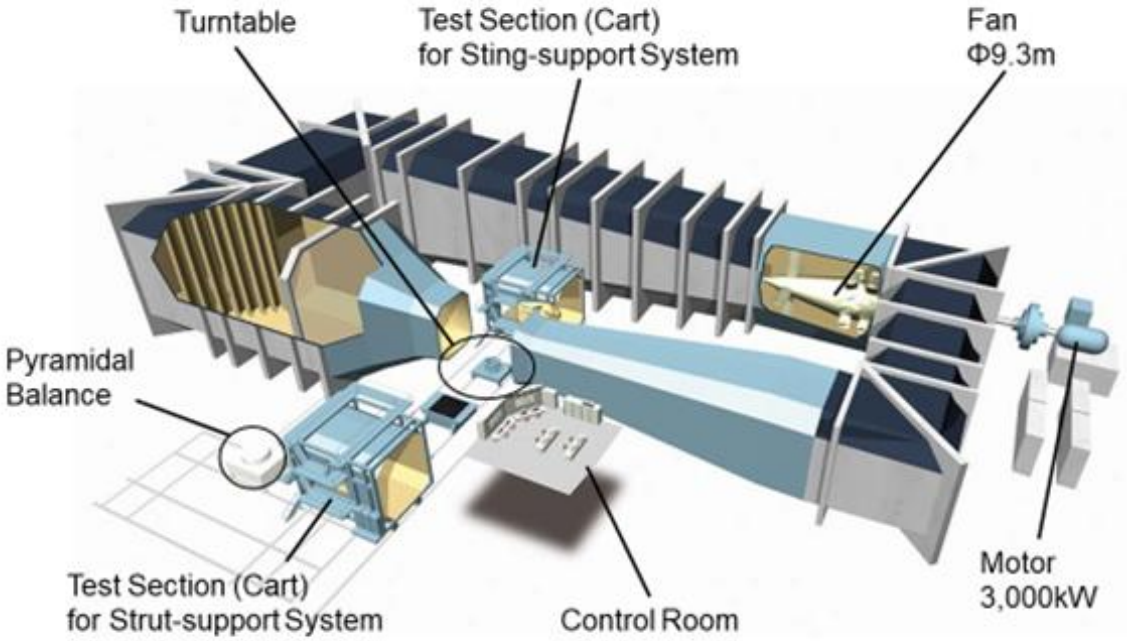


Figure 1 - The schematic of the JAXA LWT1.

Table 1 - Specification of the JAXA LWT1.

Item	Performance
Type	Atmospheric pressure closed-circuit
Wind speed	1 to 70 m/s
Fan	Rotating speed and variable pitch angle control
Test section size	Height: 6.5 m, Width: 5.5 m, Length: 9.25 m, Octagonal with corner truncated 1 m
Test section cart	Strut cart, Sting cart, Open cart
Construction	1965

3. Model Description

3.1 Model Specification

Table 2 shows the dimensions of the CRM-HL model fabricated by JAXA. The model scale is 8% of the original design shape, representing a semispan model of the starboard side. This model was designed for use in JAXA LWT1. The semispan length is roughly the same as the JSM model [12]. The model scale was selected to allow for noise source measurement tests to be conducted in the low-speed wind tunnel of Kawasaki Heavy Industries (KLWT) [13], with which JAXA is conducting collaborative research. The model surface is painted glossy black for optical measurements. The model consists of slats, flaps, main wing, fuselage, nacelle pylon, horizontal tail, and main landing gear. The model can be tested with nacelle pylon, horizontal tail, and main landing gear removed. Most of the model parts are manufactured of aluminum alloy, and the standard slat support brackets, device slats, device slat support brackets, and fuselage core, that require high strength, are made of steel.

Table 3 shows the slat and the flap angle settings. The configurations defined in the CRM-HL ecosystem are compatible with landing and takeoff configurations, and the landing configuration also supports a configuration for low Reynolds numbers with a flap angle three degrees lower. The flaps can also be configured for cruise flights. Furthermore, when determining the CRM-HL reference configuration, NASA first produced a 10% CRM-HL semi-span model, and the data from this model was analyzed to determine the reference configuration by Boeing [14]. NASA has used the original 10% semi-span model to acquire noise data [15]. To compare with this data, our model can also be

tested with the same configuration.

Table 2 - Model dimensions.

Item	Dimensions
Scale	8%
Type	Semispan
Length	5.018m
Semispan length	2.351m
Reference area	1.238m2
Reference cord	0.560m

Table 3 - Slat and Flap setting.

Objective	Configuration	Slat angle, degree	Inboard flap angle, degree	Outboard flap angle, degree
CRM-HL Ecosystem Reference data	Landing	30	40 37	37 34
	Take off	22	25	25
	Cruise	-	0	0
NASA 10% SS model noise source data	Landing	30	37	37

3.2 Model shape definition

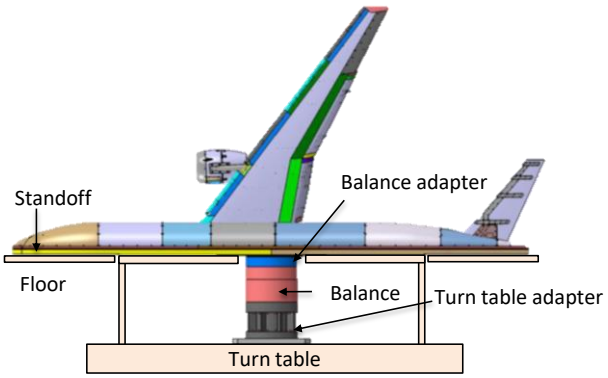
For model fabrication, geometry data was obtained from the NASA website Reference Geometry [16]. The trailing edge thicknesses of the wing, slats, flaps, and tail were available in either 0.20 in or 0.40 in sizes, but 0.20 in was selected for the larger model. Since the slat support brackets and flap fairings were not published on the website, the NASA 5.2% semi-span model's geometry was obtained [17]. The wingtip and aileron separation positions were also similar. While there is a shared shape for the flap fairing in the reference geometry, it was still under design at the time of our model construction. We fabricated it with the same shape of the NASA 5.2% semi-span model used to obtain high Reynolds number data.

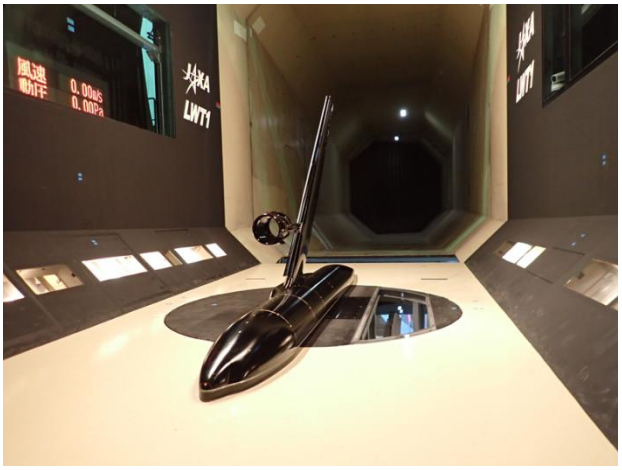
The NASA noise data comparison configuration differs from the reference configuration in terms of slat placement, slat support bracket shape, flap steering angle, flap fairing shape, and nacelle lip shape, so the geometry obtained directly from NASA was designed to be interchangeable with the reference configuration.

Although a simplified main landing gear shape is defined as a reference shape, we wanted to conduct research into reducing noise in the main landing gear using a detailed shape, so we used the main landing gear shape obtained directly from NASA during the noise data collection campaign [15].

3.3 Model design and fabrication

Figure 2 shows the 8%CRM-HL semi-span model installed at the test section in JAXA LWT1. The mounting base of the fuselage is fixed to the tunnel turntable of the test section with a turntable adapter, a five-component balance, and a balance adapter. To reduce the influence of the boundary layer on the wind tunnel floor, a standoff or peniche, which elevates the fuselage symmetry plane, is fixed to the floor as shown in Figure 3. A labyrinth shape is formed between the standoff and the fuselage symmetry plane to prevent the aerodynamic forces acting on the standoff and affecting the aerodynamic force measurements. Two standoffs with heights two and four times the displacement thickness of the floor boundary layer at LWT1 are prepared. The heights include the labyrinth seal distance. In a preliminary measurement of the floor boundary layer, the displacement thickness at the floor center was approximately 15 mm over a wind speed range of 50–70 m/s. For this reason, the standoffs with heights of 30 mm and 60 mm were fabricated. Additionally, a configuration, with a gap between the fuselage symmetry plane and the floor can also be set, potentially reducing the influence of the boundary layer on the floor [18].





(a) Design shape of model installation (b)Model installed in the test section

Figure 2 - Model installation.

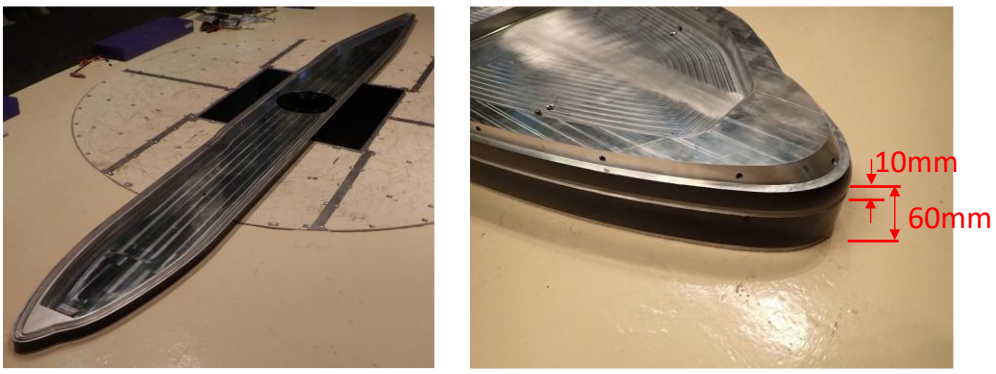


Figure 3 - Standoff and symmetrical plane of the fuselage.

The main wing configurations are shown in Figure 4. The leading edge of the wing is equipped with inboard and outboard slats, and the trailing edge with inboard and outboard flaps. The outboard slat is divided into three parts for ease of fabrication and installation. This division is also considered acceptable as a reference shape definition [2]. Two sets of slats were fabricated. One is standard slats with pressure taps and unsteady pressure sensors, and the other set consists of slats designed for the installation of noise reduction devices without pressure taps and transient pressure sensors. The device slats are split to change the trailing edges and have tapped holes on the lower surfaces for the installation of the noise reduction device. The trailing edge of middle slat (#2 slat) of the outboard slat is split into nine sections in the span direction to change the trailing edge length individually. This allows for individual selection of trailing edge lengths near and away from the bracket. The flap configuration is shown in Figure 5. The outboard side of the inner flap and both ends of the outer flap are interchangeable, allowing for the installation of noise reduction devices and other modifications. Flap deflection angles can be changed by replacing the support brackets.

This model can be used with and without a nacelle and pylon, as shown in Figure 6. The configuration with nacelle and pylon is considered the baseline configuration. A slat adapter connected with inner and outer slats was also fabricated to enable testing with the nacelle removed. The nacelle chine is also removable. The nacelle lip is exchangeable to the same one used in the NASA 10% semispan model.



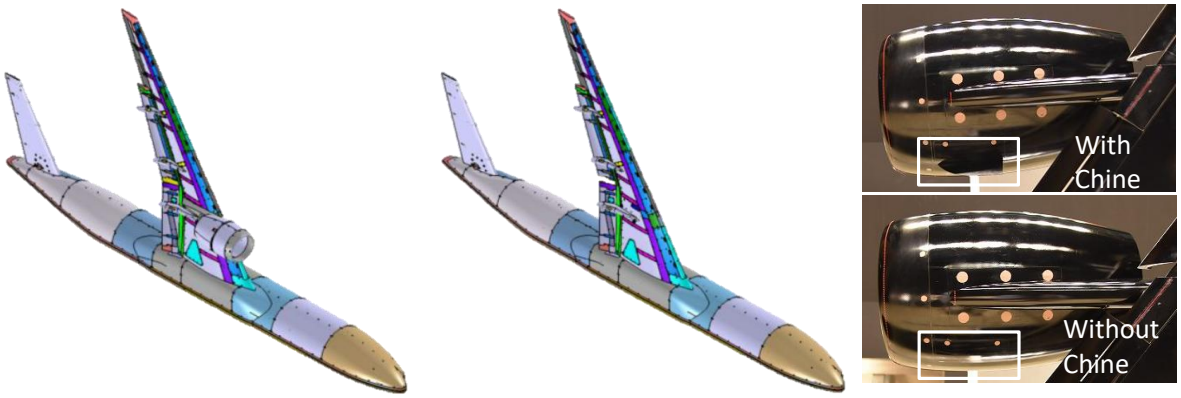
(a)Standard slats (b)Device slats (c)Support brackets

Figure 4 - Main wing configuration.



(a)Main wing (b)Flaps (c)Support brackets (FTF)

Figure 5 - Flap configuration.



(a)With nacelle and Pylon (b)Without nacelle and pylon (c)With and without chine

Figure 6 - Nacelle and pylon configurations.

The main landing gear configuration is shown in Figure 7. It is an 8%-scale model of a four-wheel main landing gear designed by NASA. Total height is approximately 450 mm, and the tire diameter is approximately 110mm [9]. Most of the main landing gear parts are made of plastic using stereolithography, but metal components are used for the core parts. It can be installed in the cavity under the wing. Wind tunnel tests can be conducted without main landing gear and closing the cavity area.

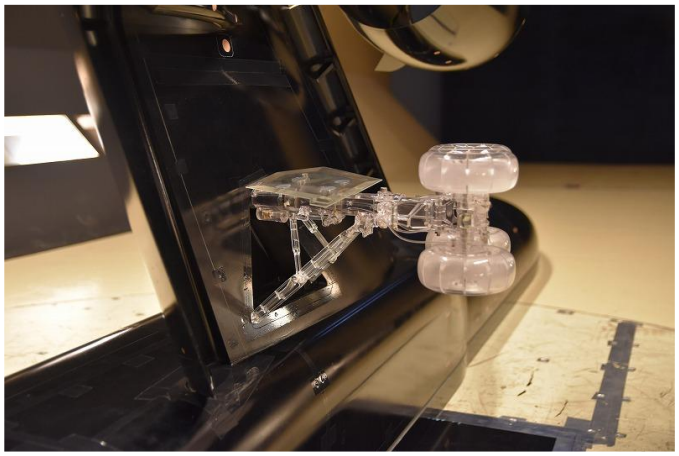


Figure 7 - Main landing gear configuration.

3.4 Pressure taps and unsteady pressure sensors

Table 4 lists the pressure holes on the model surface, and Figure 8 shows their relationship to the wing pressure hole cross-section locations defined in the CRM-HL Ecosystem. Due to constraints on both wind tunnel pressure measurement system and model, eight pressure hole cross-sections (A-D, F-I) were selected from the 10 defined in the ecosystem (A-G), for a total of 433 pressure points. Thirty-one points were located on the fuselage, 159 on the main wing, 92 on the slats, 84 on the flaps, 15 on the nacelle, and 52 on the horizontal stabilizer. The pressure hole cross-section locations on the upstream main wing and slats are perpendicular to the leading edge.

Sixteen unsteady pressure sensors were installed on the model as shown in Figure 9. As unsteady pressure sensors, Kulite's pressure sensors are mounted at five points on the upper surface of the main wing and flaps, five points on the cove surface of the #2 slat, five points on the leading edge of the main wing corresponding to the #2 slat, and one point on the upper surface of the horizontal stabilizer.

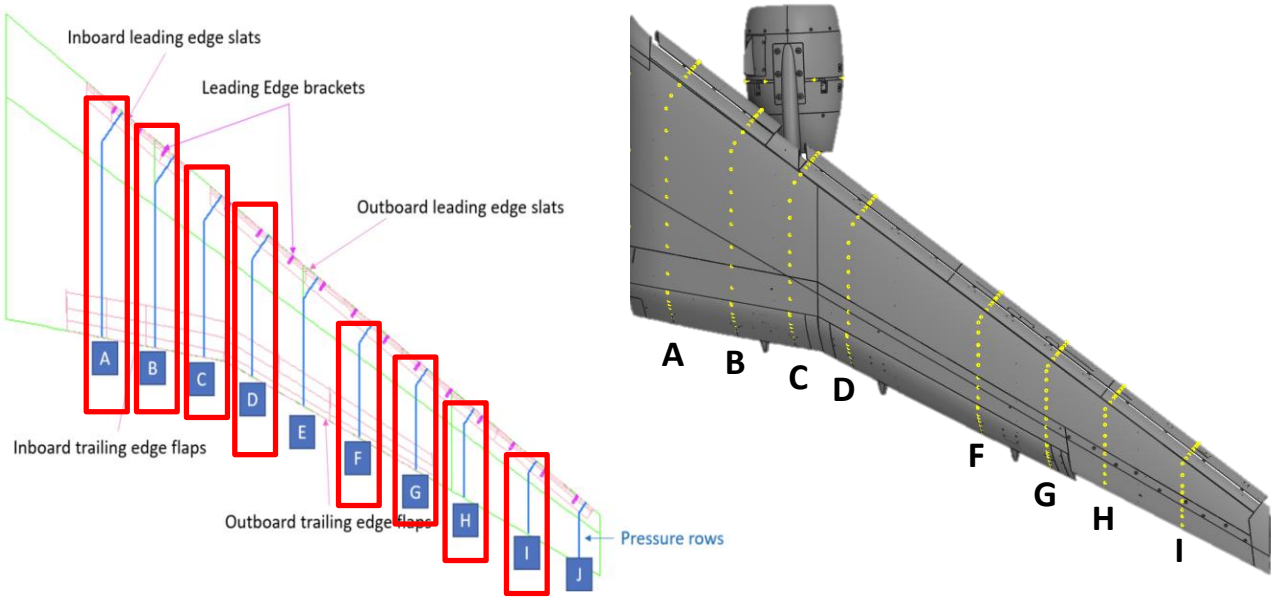


Figure 8 - Correspondence with pressure hole cross sections defined in the CRM-HL Ecosystem (JAXA model has A to D and F to I section).

Table 4 - Location of pressure ports.

Parts	Detailed parts	Location	Number
Fuselage	—	0.05, 0.15, 0.25, 0.3, 0.35, 0.4, 0.45, 0.5, 0.55, 0.6, 0.7Length	31
Wing	—	η=0.160 (A) η=0.251 (B) η=0.333 (C) η=0.415 (D) η=0.596 (F) η=0.692 (G) η=0.774 (H) η=0.882 (I)	159
Slat	Inboard Slat	η=0.160 η=0.251	92
	Outboard Slat#3	η=0.333 η=0.415	
	Outboard Slat#2	η=0.596 η=0.692	
	Outboard Slat#1	η=0.774 η=0.882	
Flap	Inboard Flap	η=0.160 η=0.251 η=0.333	84
	Outboard Flap	η=0.415 η=0.596 η=0.692	
Nacelle	Outer surface	30-330°(Δ60 °)	15
	Inner surface	0-270°(Δ90°)	
	Total pressure	Center, 45-315°(Δ90°)	
Horizontal tail	—	η=0.30 η=0.60 η=0.80 η=0.95	52
Sum	—	—	433

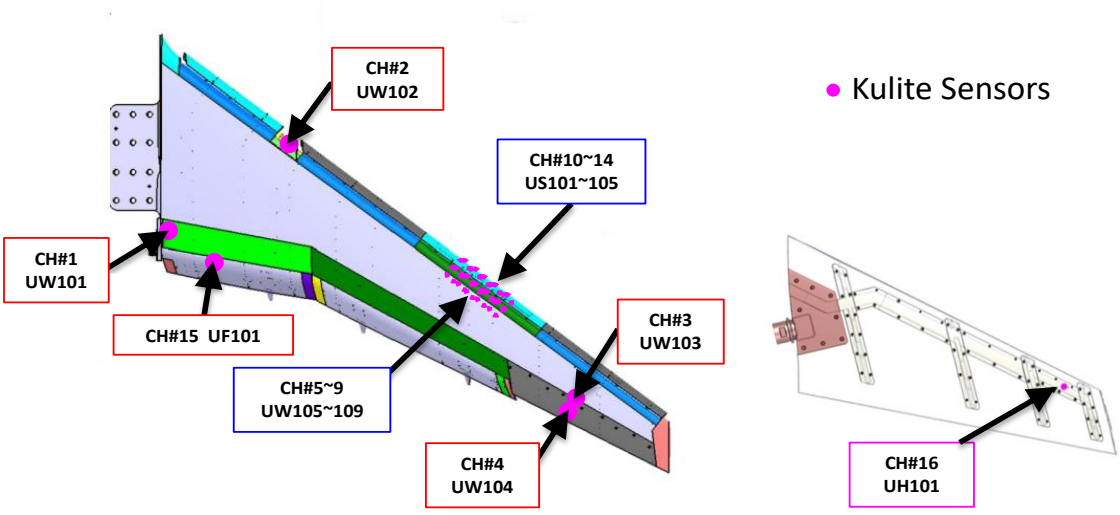


Figure 9 - Location of the unsteady pressure sensors.

4. Wind tunnel test overview

4.1 Test contents

The first wind tunnel test following the delivery of the 8%CRM-HL semi-span model was conducted at JAXA LWT1 from April to May 2025 by the FQUROH-2 team. The objectives of this test were to confirm the functionality of the newly installed wind tunnel model, acquire aerodynamic data, and verify the noise reduction effects of the high-lift devices and the main landing gear.

The second wind tunnel test was conducted at LWT1 from October to December by the Off-Design Aerodynamics Team. The purpose of this test was to clarify the aerodynamic phenomena in the stall region of the high-lift configuration and to obtain data for the development of stall prediction technologies.

The third wind tunnel test was conducted at LWT1 from February to March 2026 by the FQUROH-2 team. The objectives of this test were to perform acoustic and aerodynamic evaluations of low-noise concepts for high-lift devices and the main landing gear, to assess the effects of noise directivity, and to acquire data for a model configuration corresponding to the NASA 10% semi-span wind tunnel test.

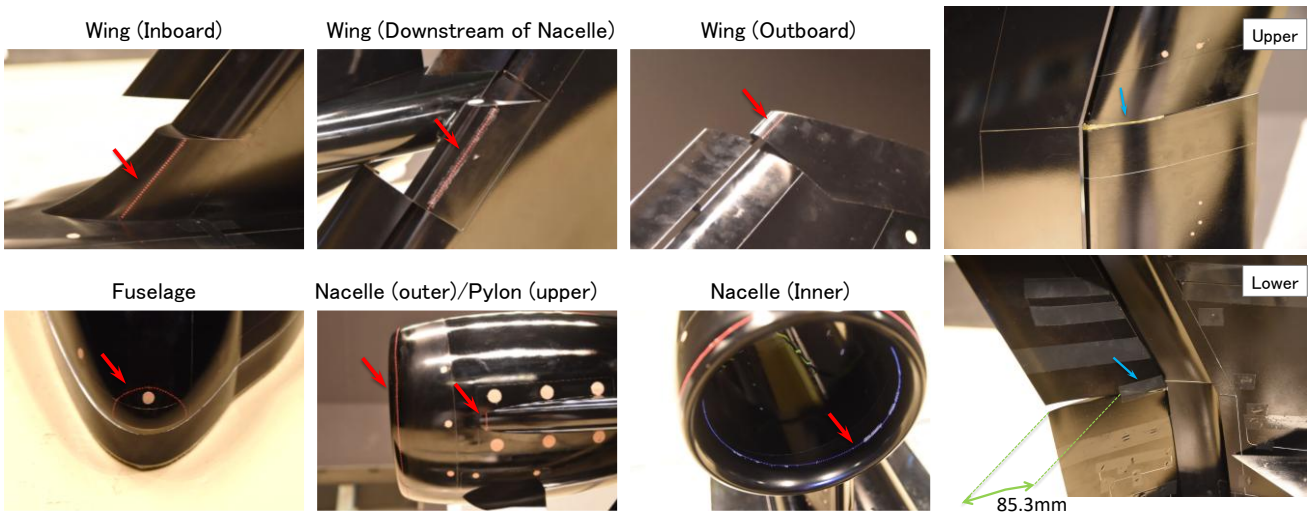
The test conditions were primarily a Mach number of 0.2, with data also obtained at Mach numbers of 0.18, 0.16, and 0.15. The angle of attack ranged from -5 to 21 degrees. During the Mach number 0.2 test, the temperature in the airflow ranged from 14 °C to 31 °C, resulting in wind speeds ranging from 68 m/s to 70 m/s, and Reynolds numbers based on wing chord length ranging around 2.5×10^6.

4.2 Model condition and preparation

The wind tunnel tests were conducted using the CRM-HL ecosystem reference configuration and NASA 10% semispan configuration for landing. The model was set on a 60-mm-high standoff to minimize interference between the model and the boundary layer on the test section floor. The height of the standoff had been determined based on CFD simulations and previously conducted wind tunnel tests with the JSM model [12]. The locations and heights of disc roughness for forced transition are shown in Table 5 and Figure 10. They were installed on the upper surfaces of the wings that are not downstream of the slats, nose, inner and outer nacelle sides, pylons, and upper and lower surfaces of the horizontal tail. Disc roughness heights based on past wind tunnel tests were used [19]. The flap gap between the inboard flap and the outboard flap is filled by beeswax from the leading edge to 85.3 mm forward of the IB flap trailing edge. The screw holes on the model were filled with clay and shaped. The areas with little aerodynamic effect, such as the under surface of the wing, were sealed with black scotch tape.

Table 5 - Locations and heights of disc roughness.

Parts	Detailed parts	Location, mm	Height, mm
Wing	Inboard	22.7	0.251
	Downstream of the nacelle	22.8	0.251
	Outboard	10.6	0.251
Fuselage	Nose	19.0	0.251
Nacelle	Outer	12.2	0.251
	Inner	50.2	0.290
Pylon	Upper	10.0	0.251
Horizontal tail	Upper and lower	37.5	0.251



(a) Locations of disc roughness. (b)Flap gap filling.

Figure 10 – Model surface treatment.

4.3 Measurement items

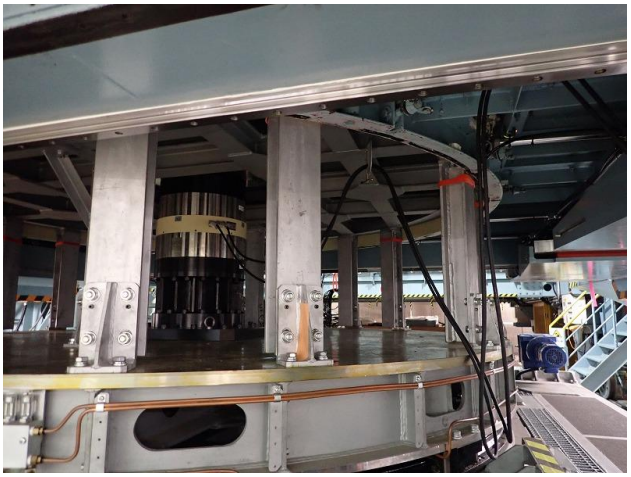
In the first and third wind tunnel test series, measurements of forces and moments, surface pressure distributions, unsteady pressures, and aeroacoustic data were conducted. Tuft flow visualization was performed only during the first test series. These tests primarily focused on airframe noise measurements. Airframe noise measurements were primarily conducted from angle of attack of 0 degrees to 12 degrees, while aerodynamic characteristics data was obtained up to 21 degrees. In the present paper, only the aerodynamic data related to the stall phenomenon are reported. In the second test series, aerodynamic measurements, surface pressure measurements, oil flow visualization, and PIV measurements were carried out with a focus on stall phenomena. Oil flow and PIV measurements were mainly performed around an angle of attack of 17 degrees, corresponding to the expected stall condition.

Forces and moments were measured using a five-component balance, as shown in Figure 11. Surface pressure distributions were measured using seven modules of an electronically scanned pressure (ESP) system equipped with digital temperature compensation. Unsteady pressures were recorded with a sampling frequency of 200 kHz and a low-pass cutoff frequency of 100 kHz, resulting in a total of 1,600,000 samples. For oil flow visualization, a mixture of silicone oil and fluorescent pigment was applied to the wing and fuselage surfaces. The oil flow patterns were illuminated using three black lights and recorded by a camera mounted on the side window of the test section.

Steady two-dimensional, three-component stereoscopic PIV measurements were performed on planes perpendicular to the model centerline. An overview of the PIV measurement setup is shown in Figure 12. An acrylic window was installed on the turntable on the upper-surface side of the model. Two PIV cameras and a laser were mounted on a traverse mechanism located below the window. By installing the optical system inside the turntable, the equipment moves along with the model's attitude angle. This allows for measurement of the same cross-section on the model's axis, even when the attitude angle changes. The traverse was moved 400 mm upstream and downstream of the aerodynamic center to capture the nacelle wake over the upper surface of the wing. PIV measurements were conducted by injecting oil mist downstream of the test section and circulating it with low-speed airflow to ensure a uniform particle distribution. Sebacic acid was used as the seeding material. A total of 2000 image pairs were acquired at a sampling frequency of 8 Hz. Laser reflections from the model surface caused spurious signals in the vicinity of the model. These regions were identified and excluded from the PIV analysis by applying an image mask. Although the masking procedure significantly reduced the influence of reflections, some residual effects remain in limited areas. Velocity data in these regions were therefore not used for flow interpretation.

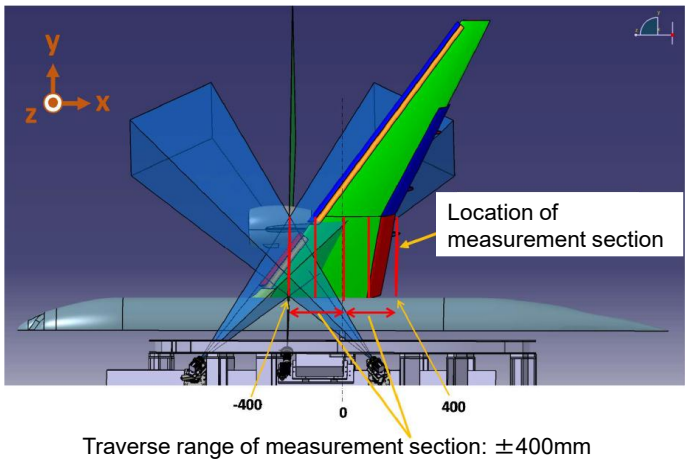


(a)Balance shape

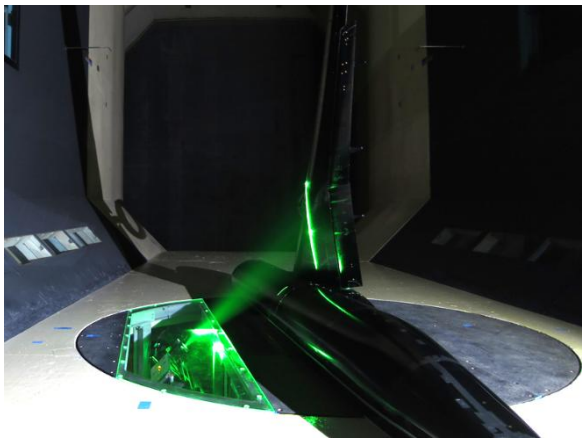


(b)Balance installed in the turntable

Figure 11 - Five-component balance.



(a)PIV Measurement Equipment Placement



(b)Picture of the PIV set up

Figure 12 – PIV measurement set up.

5. Test results

5.1 Force and moment measurements

Figure 13 shows five aerodynamic coefficient data sets obtained from three wind tunnel test series, including repeated runs, for the reference configuration (Chine ON, H-tail OFF) at a Mach number of 0.2. The first four digits of the graph series name represent the test series name, and the last three digits represent the run number. Wall interference corrections were applied to these test data. For the reference con figuration, lift coefficient (CL) increases linearly up to approximately 6.4 degrees. The lift slope then gradually decreases beyond around 8.4 degrees. In many datasets, the CL reaches its maximum value (~2.3) at approximately 17.5 degrees. A decrease in CL is observed at angles of attack greater than this, indicating that the wing has exceeded its critical angle of attack and entered full stall. Therefore, in the following discussion, we will consider 17.5 degrees as the angle of attack at CL max. Drag coefficient (CD) increases with increasing angle of attack and increases further after stall. The pitching moment coefficient (Cm) continues to increase with increasing angle of attack even after stalling, up to around 19.0 degrees, and then decreases thereafter. The separation on the wing surface at angles of attack after maximum lift occurs in the wake beyond the moment reference point, and at angles of attack greater than approximately 19 degrees, the separation region is thought to extend upstream of the moment reference point.

To quantitatively evaluate data reproducibility, Figure 14 presents the standard deviations of three data sets obtained within a single wind tunnel test series (in-test reproducibility) and of five data sets acquired from three different test series (inter-test reproducibility). Regarding in-test reproducibility, at low angles of attack (−5 degrees to +15 degrees), where flow separation over the wing is limited,

the standard deviations are generally small, remaining below 0.005 for CL and below 5 drag counts for CD. At higher angles of attack, where flow separation becomes more pronounced, the standard deviations increase; however, the variations remain within acceptable ranges (ΔCL = 0.01, ΔCD = 0.002, ΔCm = 0.01) for aerodynamic analysis. With respect to inter-test reproducibility, the standard deviations of CD and Cm are approximately twice those of the in-test reproducibility, which is considered reasonable for wind tunnel testing. For CL, a slightly larger standard deviation of approximately 0.01 is observed around an angle of attack of 10 degrees. This increase may be attributed to uncertainties in the initial angle-of-attack setting, model assembly tolerances, and model surface accuracy. Further evaluation will be performed as additional wind tunnel test data become available.

Figure 15 compares the aerodynamic coefficient variations with angle of attack for the reference configuration (Chine ON, H-tail OFF) and the configuration without chine (Chine OFF, H-tail OFF) at a Mach number of 0.2. The lift for the chine-off configuration begins to decrease compared to the reference configuration around 12.5 degrees and is approximately 0.1 lower at high angles of attack. This result suggests that the chine installation on the nacelle contributes to the suppression of wing flow separation.

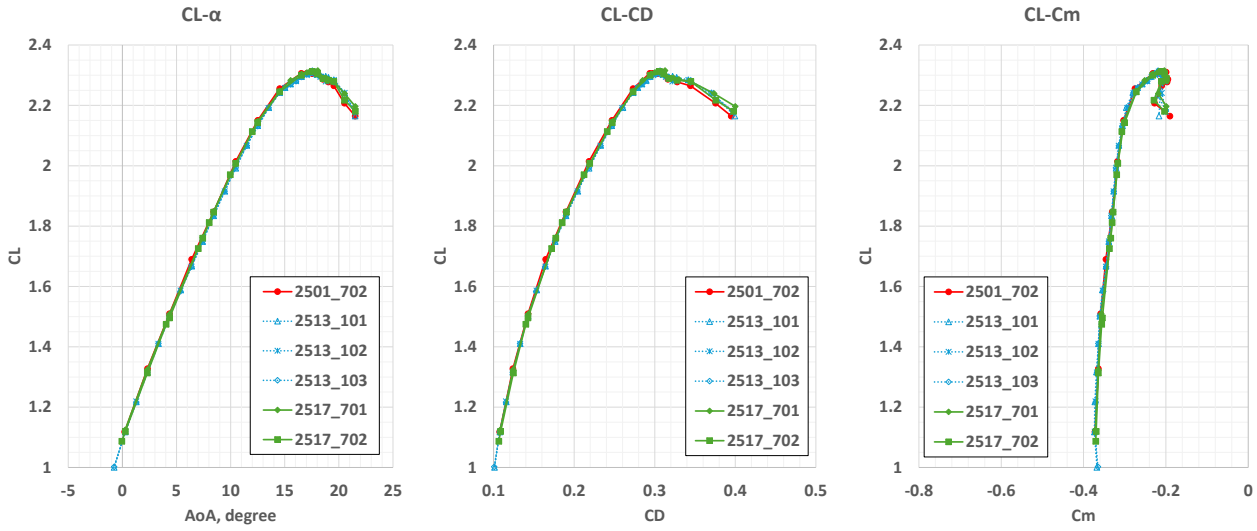


Figure 13 – Forces and moments (Landing configuration at M=0.2, Re=2.5million).

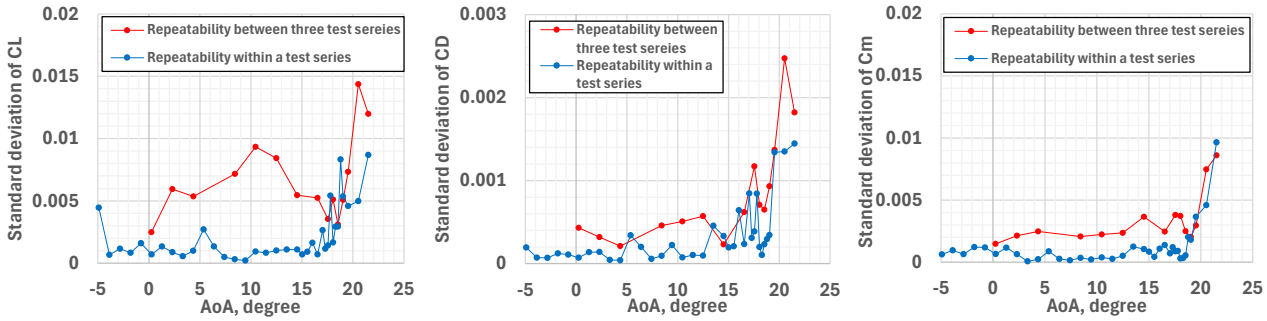


Figure 14 – In-test and Inter-test repeatability (Landing configuration at M=0.2, Re=2.5million).

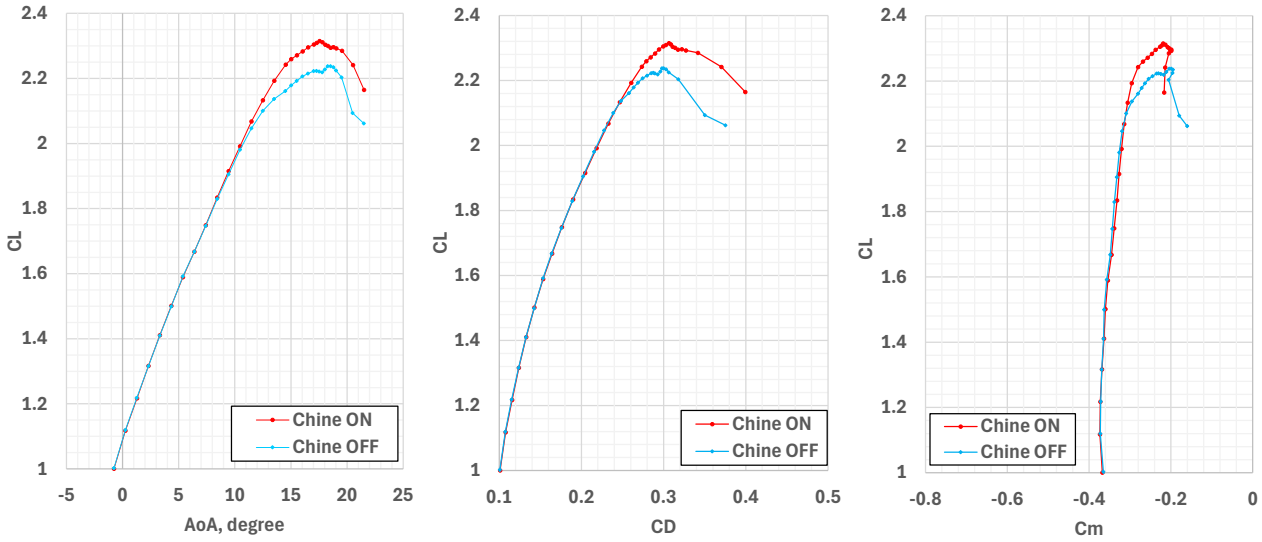


Figure 15 – Chine effect of forces and moments (Landing configuration at M=0.2, Re=2.5million).

5.2 Pressure distributions

Figure 16 shows the pressure coefficient (Cp) distribution measured under standard conditions at a Mach number of 0.2 for the reference configuration (Chine ON, H-tail OFF). The horizontal axis represents the ratio of the axial length between the leading and trailing edges of each wing section (slats and flaps retracted) to 1. For the flaps, suction decreases as the angle of attack increases from section A to section G. From section A to section C, suction decreases sharply from an angle of attack of 17.5degrees, and from section B to section D, suction decreases further at an angle of attack of 20.5 degrees. For the wing, leading edge suction increases from section A to section C up to an angle of attack of 17.5 degrees and then decreases after stall. For the slats, suction increases as the angle of attack increases in almost all sections.

Figure 17 compares the pressure coefficient distribution at sections A-D, corresponding to the chine wake on the inner side of the main wing, for the configuration with and without a nacelle chine, at Mach 0.2 and an angle of attack of 17.5 degrees. In the configuration without chine, the lift from the main wing and flaps is significantly lower, and the slat suction peak is larger. This indicates that a larger proportion of the total lift is generated by the slats. In contrast, in the configuration with chine, the chine reduces separation on the upper surface of the main wing, maintaining the lift generated by the main wing and flaps even at high angles of attack.

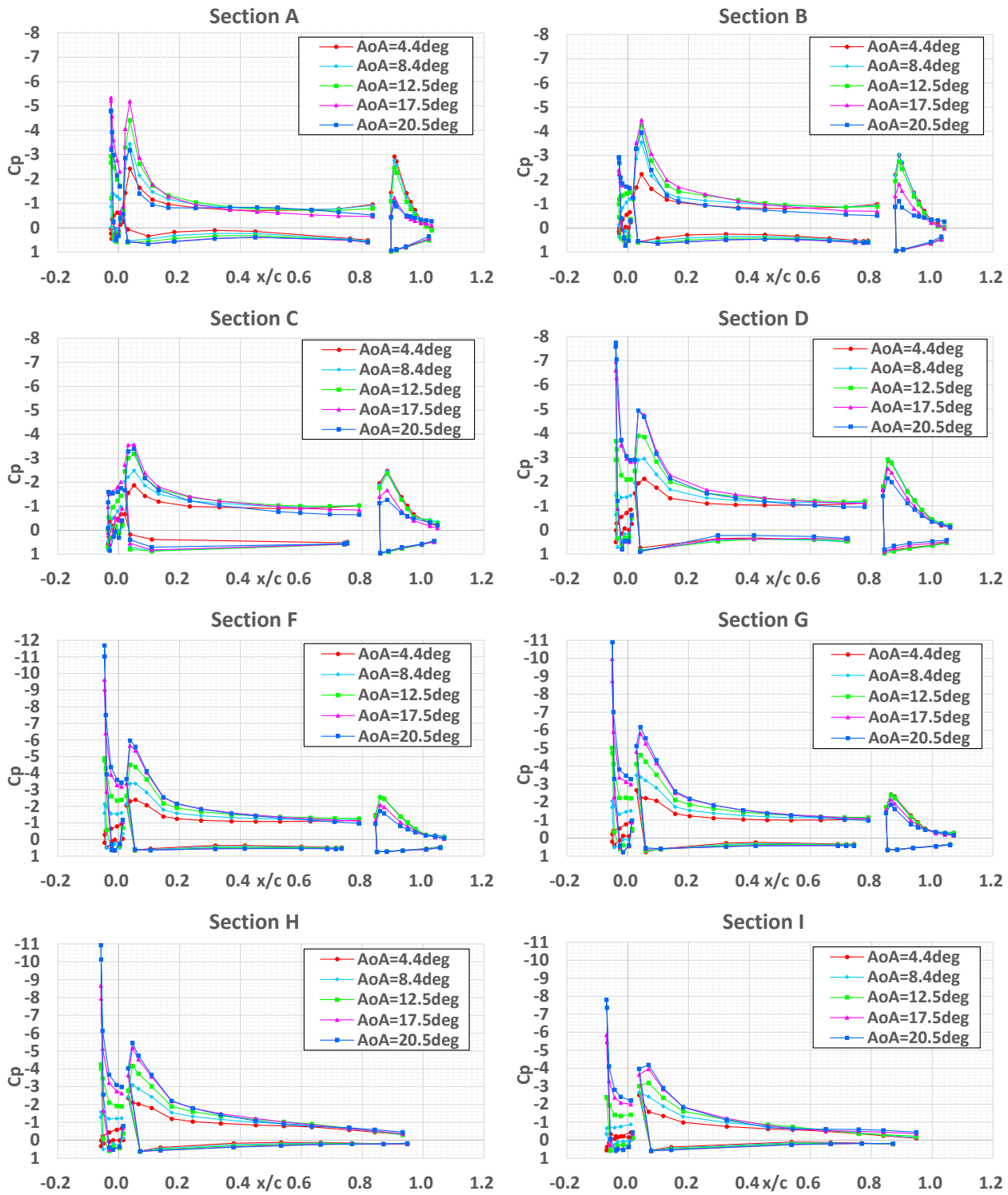


Figure 16 – Pressure coefficient distributions on the wing (Landing configuration at M=0.2, Re=2.5million).

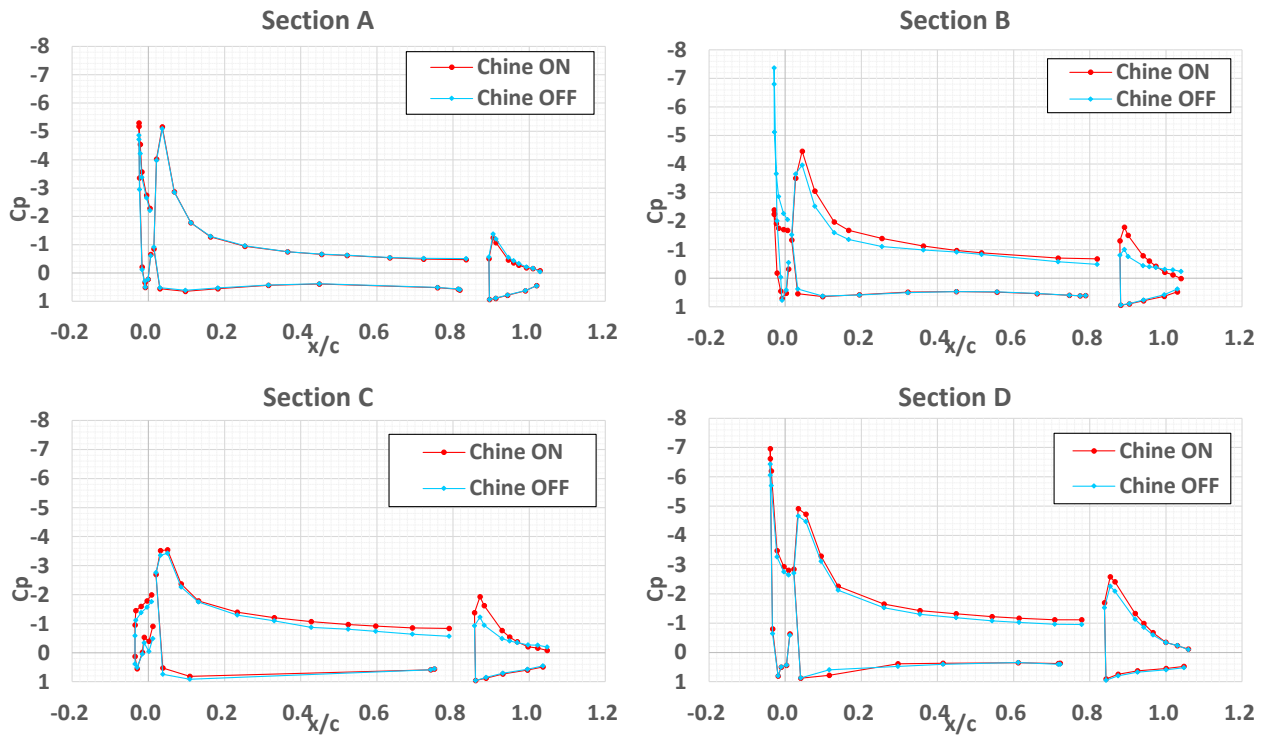
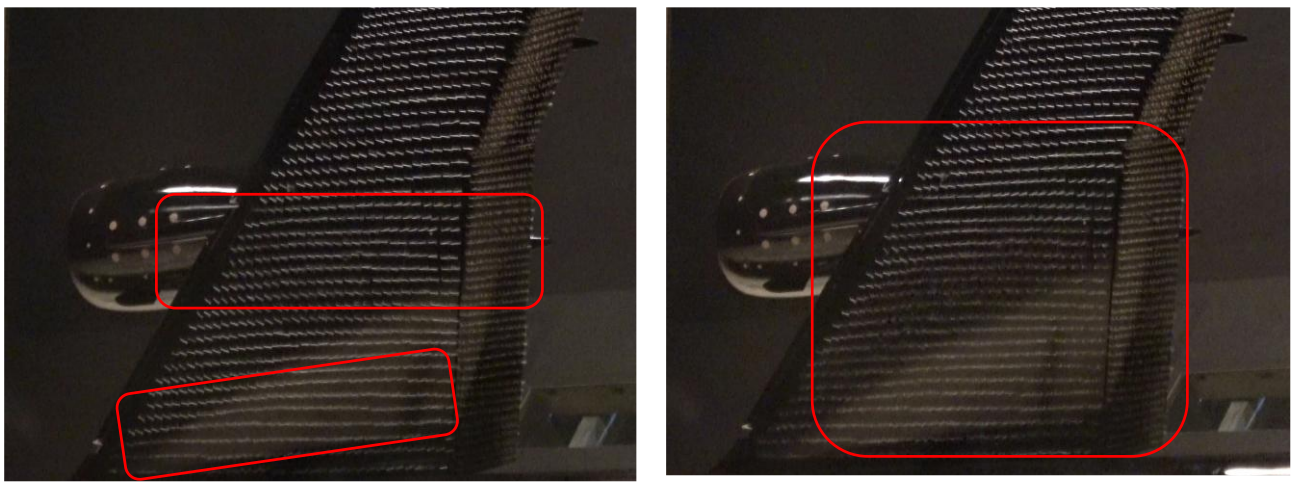


Figure 17 – Chine effect of pressure coefficient distributions on inboard side of the wing (Landing configuration at M=0.2, Re=2.5million, AoA=17.5deg).

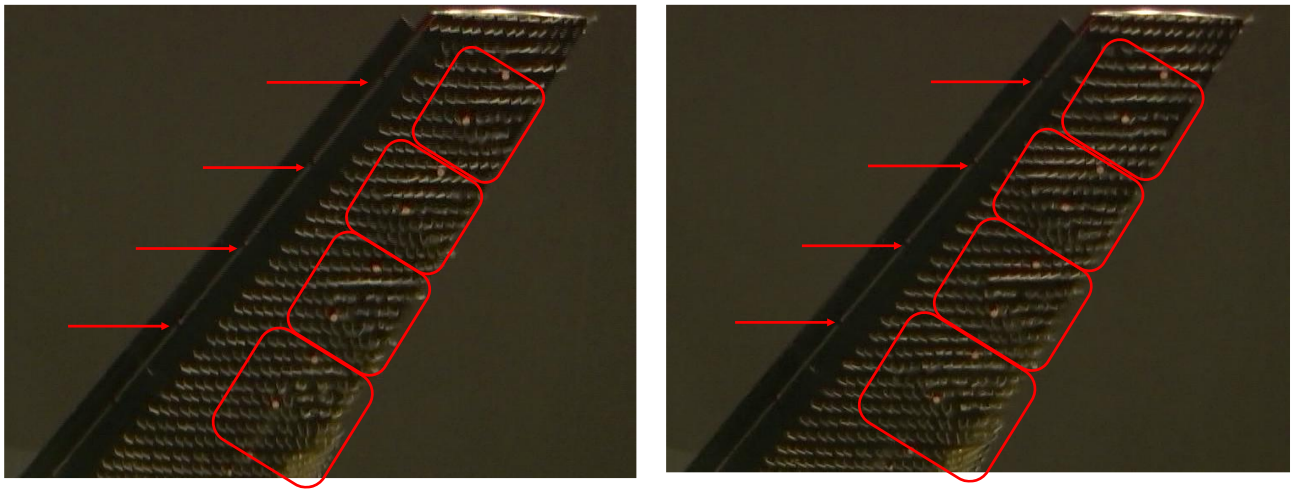
5.3 Tuft visualization

Figure 18 shows the results of the tuft visualization on the upper surface of the wing for the CL-max angle of attack of 17.5 degrees and a post-stall angle of 20.5 degrees. In the inboard side of the wing, the turbulent region in the wake of the nacelle increases after stall. Also, on the outboard side of the wing, the triangular turbulent region in the wake of the slat support expands after stall. The expansion of the turbulent region on the inboard side has a large effect on stall.



(a) Inboard at AoA=17.5deg

(b) Inboard at AoA=20.5deg



(c) Outboard at AoA=17.5deg (d) Outboard at AoA=20.5deg

Figure 18 – Tuft visualization (Landing configuration at M=0.2, Re=2.5million).

5.4 Oil flow visualization

Figure 19 shows the oil flow results for attitude angles from 8.4 degrees to 20.5 degrees. The separation region in the wake of the outer side support fittings expands as the attitude angle increases. Although separation on the inner flaps is observed at low angles of attack in the oil flow visualization, Fig. 16 does not show a pronounced adverse pressure gradient indicative of separation, which may be at least partly attributed to differences in measurement locations and diagnostic techniques.For the outer side flaps, separation is observed in the region near the flap fairing at all attitude angles. It was found that the separation region near the fuselage, which is affected by vortices originating from the step between the leading edge of the inner chord side of the main wing and the slat storage area, gradually expands as the attitude angle increases, and further expands after stall.

Figure 20 shows the oil flow data with and without a nacelle chine. The turbulent region of the nacelle wake in the configuration without the nacelle chine is wider due to the absence of vortices in the chine wake. This suggests that the nacelle chine suppresses flow separation in the nacelle wake.

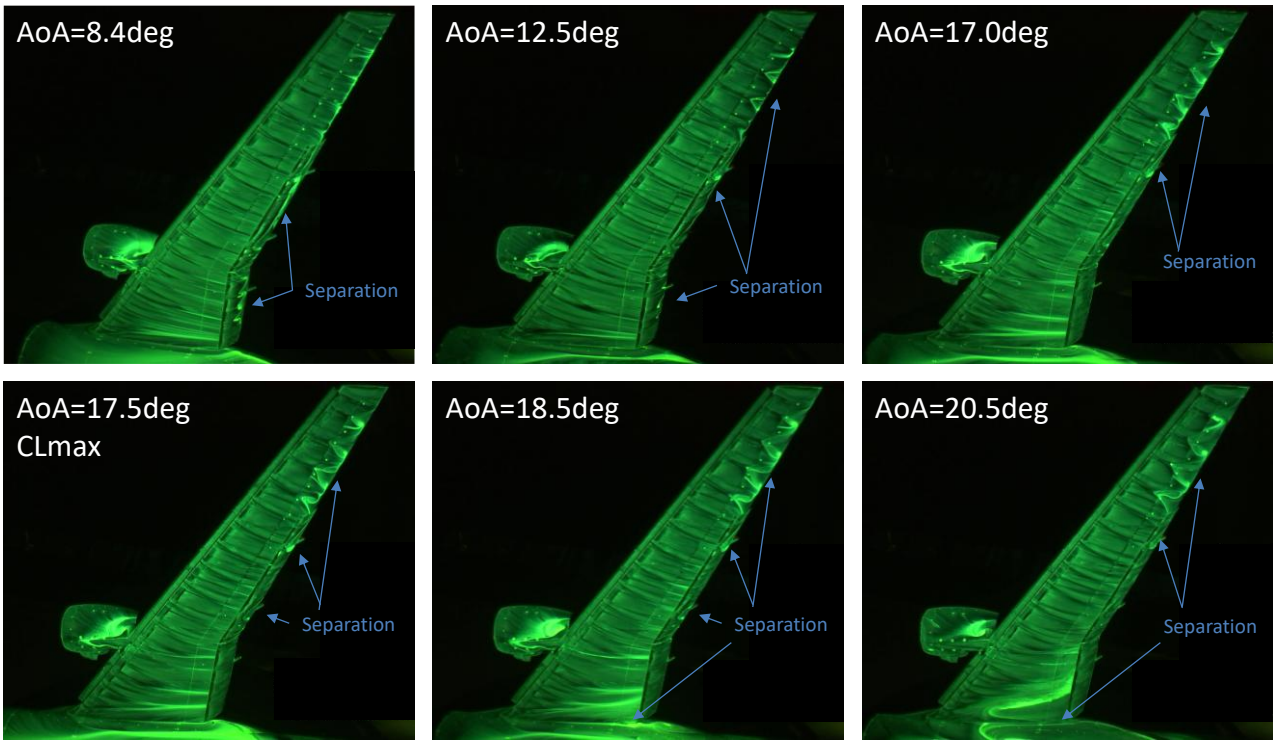


Figure 19 – Oilflow visalization results (Landing configuration at M=0.2, Re=2.5million).

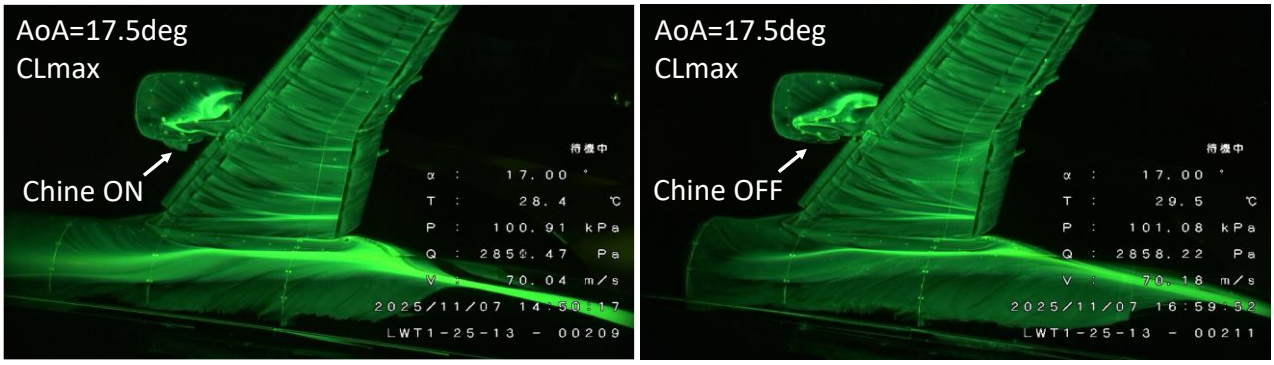


Figure 20 – Oilflow visalization with chain and without chain. (Landing configuration at M=0.2, Re=2.5million, AoA=17.5deg).

5.5 PIV measurement

Figure 21 shows the PIV analysis results of the upper wing surface at Mach 0.2 and an angle of attack of 17.5 degrees, and Figure 22 shows the results at an angle of attack of 20.5 degrees. Figure 23 shows a 3D view of similar results from an angle of attack of 8.4 degrees to 20.5 degrees. These contours indicate the ratio of the axial velocity to the uniform velocity. The vectors indicate the direction of the velocity in the YZ plane of the aircraft axis. All data uses the average of 2000 frames. Furthermore, the data at X = -400mm have been excluded from the results due to the significant influence of reflections from the model. Regions of widening vortices in the nacelle chine wake and regions of slower airflow velocity in the nacelle pylon wake are observed. As the angle of attack increases, these regions expand, and at CL max angle of attack (AoA = 17.5deg), they appear to merge near the trailing edge of the main wing. After a complete stall (AoA = 20.5deg), the influence of vortices from the step between the slat storage area at the wing root and the leading edge of the main wing is also observed. As the aircraft moves into the wake, these vortices merge with the two aforementioned regions, and a large area of low speed becomes dominant.

Figure 24 shows a comparison with similar results for the chine-less configuration at AoA = 17deg and a cross-section of X = -100mm. Due to time constraints, only data for the chine-less configuration at a cross-section of X = -100mm was obtained. It can be seen that the velocity reduction region in the nacelle pylon wake is wider, and the velocity is lower in the chine-less configuration. Regarding the velocity vectors within the YZ cross-section, with the chine present, the velocity vectors are directed towards merging with the chine vortex, but without the chine, the velocity vectors are directed away from the wing. These observations suggest that the vortices emanating from the chine are delaying the separation of the main wing.

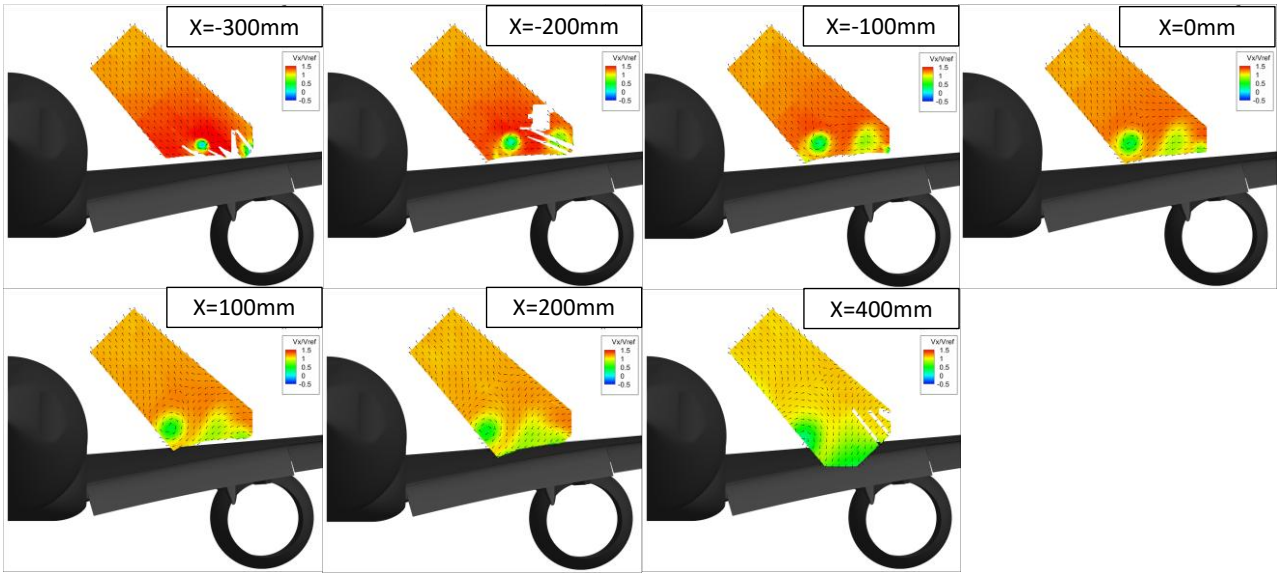


Figure 21 – PIV measurement results (Landing configuration at M=0.2, Re=2.5million, AoA=17.5deg). Regions affected by model surface reflections are masked out.

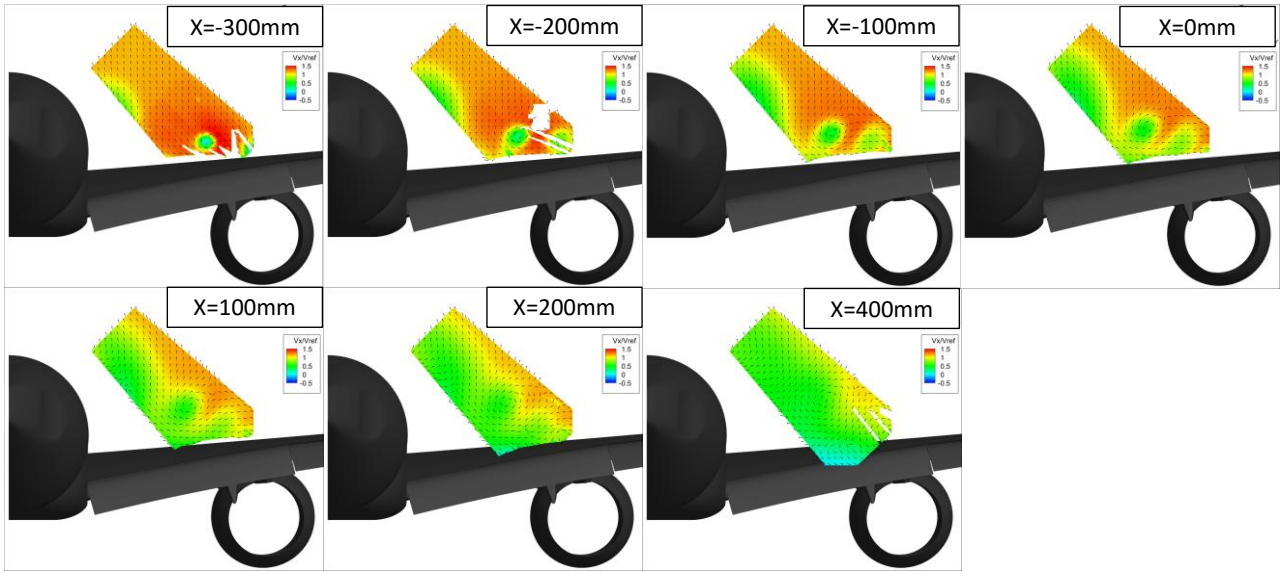


Figure 22 – PIV measurement results (Landing configuration at M=0.2, Re=2.5million, AoA=20.5deg). Regions affected by model surface reflections are masked out.

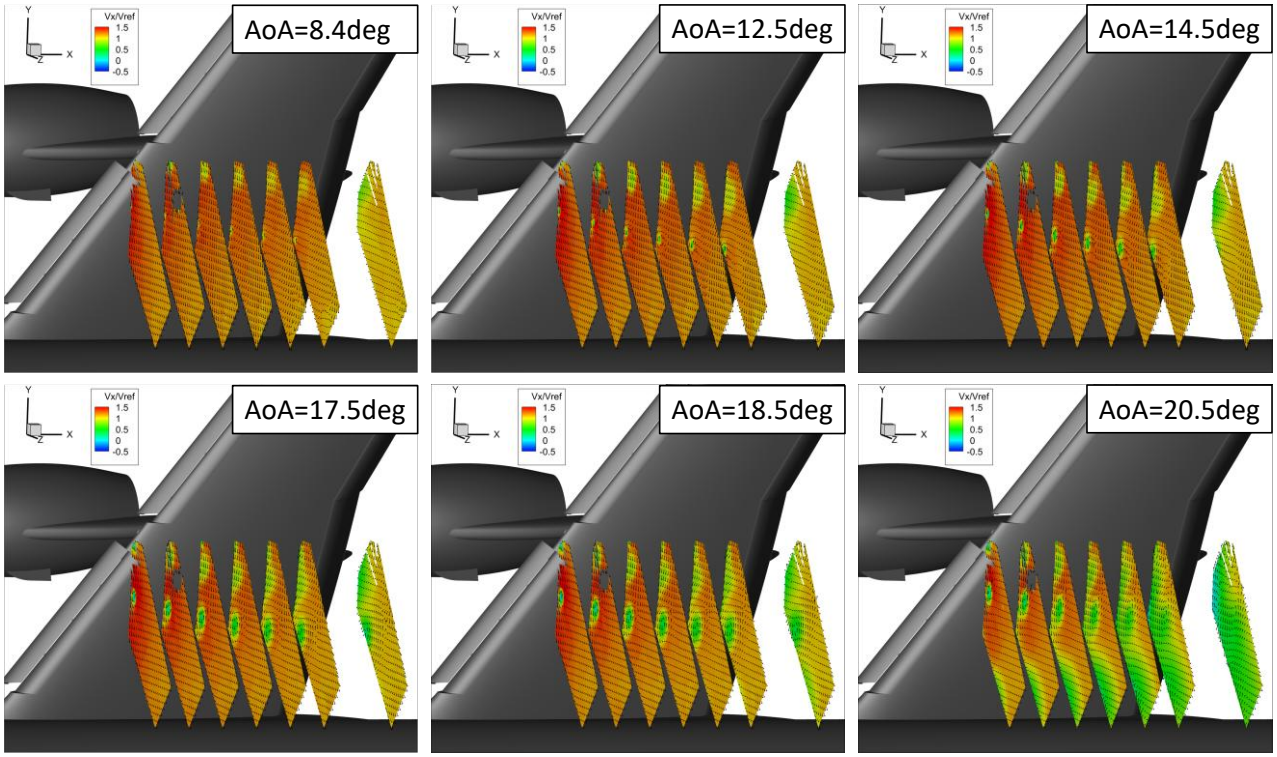
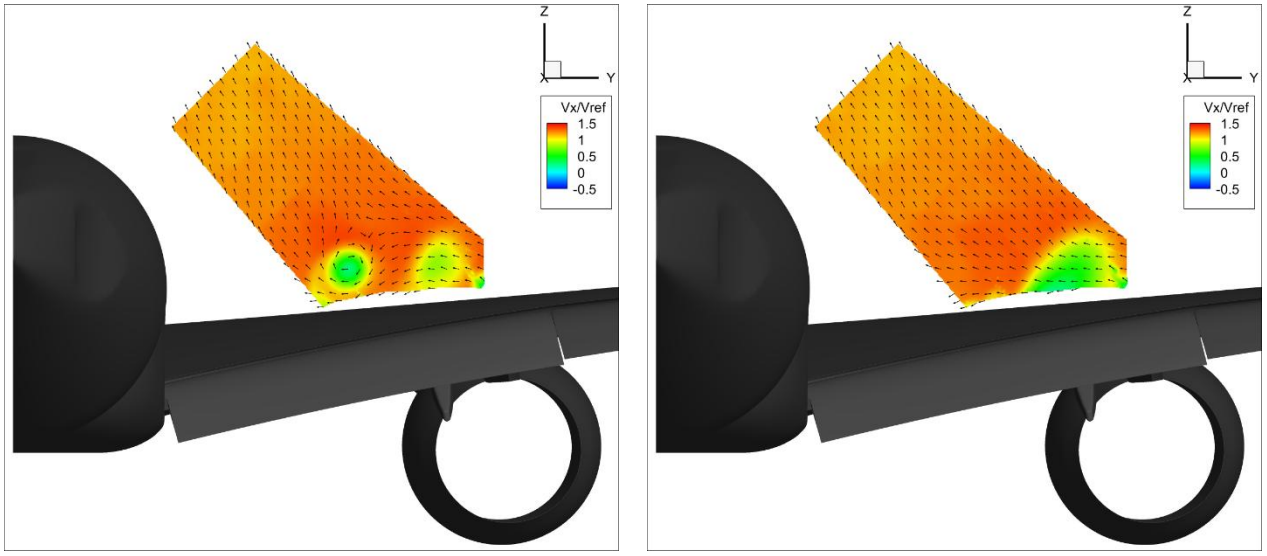


Figure 23 – 3D view of PIV measurement results (Landing configuration at M=0.2, Re=2.5million). Regions affected by model surface reflections are masked out.



(a)With chine configuration (b)Without chine configuration

Figure 24 – PIV measurement result comparison with chine and without chine. (Landing configuration at M=0.2, Re=2.5million, AoA=17.5deg, X=-100mm)

6. Conclusions

JAXA participated in the international “CRM-HL Ecosystem” to support the validation of CFD tools for high-lift configurations under low-speed stall conditions. An 8% scale semi-span CRM-HL wind tunnel model was designed and manufactured, and a series of experimental campaigns was conducted in JAXA’s 6.5 m × 5.5 m low-speed wind tunnel. The present paper described the wind tunnel model, test setup, and experimental conditions, and reported the aerodynamic characteristics of the baseline CRM-HL configuration with particular focus on stall behavior. Aerodynamic force and moment measurements demonstrated good repeatability across multiple test campaigns. Flow visualization, surface pressure measurements, and PIV results clarified the progression of flow separation near stall and indicated the role of nacelle- and chine-induced vortices in delaying wing separation. The experimental data obtained in this study provide a valuable reference for CFD validation of high-lift aerodynamics near stall at low Reynolds numbers. These results are expected to contribute to ongoing CFD development and validation activities within the CRM-HL Ecosystem.

7. Acknowledgments

The authors thank M. Rivers, C. Winski, and S. Langston of NASA Langley Research Center for providing information on the CRM‑HL model and its treatment. Support in the model design and test execution by T. Hashioka and other members of Kawasaki Heavy Industries, Ltd. is also gratefully acknowledged. The authors further acknowledge K. Shimoda of IHI Aerospace Engineering Ltd., as well as K. Tanaka and T. Hirai of Ryoyu Systems Co. Ltd., for their contributions to the preparation and execution of the wind tunnel tests. Appreciation is also extended to the low‑speed wind tunnel staff for their assistance in model setup and wind tunnel operation.

8. Contact Author Email Address

mailto: kohzai.masataka@jaxa.jp

9. Copyright Statement

The authors confirm that they, and/or their company or organization, hold copyright on all of the original material included in this paper. The authors also confirm that they have obtained permission, from the copyright holder of any third party material included in this paper, to publish it as part of their paper. The authors confirm that they give permission, or have obtained permission from the copyright holder of this paper, for the publication and distribution of this paper as part of the ICAS proceedings or as individual off-prints from the proceedings.

References

[1] Lacy, D. S., and Sclafani, A. J., "Development of the High-Lift Common Research Model (HL-CRM): A Representative High-Lift Configuration for Transonic Transports," AIAA Paper 2016-0308, 54th AIAA Aerospace Sciences Meeting, 2016.

[2] Lacy, D. S., and Clark, A. M., "Definition of Initial Landing and Takeoff Reference Configurations for the High-Lift Common Research Model (CRM-HL)," AIAA Paper 2020-2771, AIAA Aviation Forum, 2020.

[3] Slotnick, J. P., "A CFD Validation Ecosystem to Advance the Prediction of Low-Speed Aerodynamics," Proc. of the 34th Congress of the International Council of the Aeronautical Sciences, 2024.

[4] Ueno, M., Kohzai, M., Koga, S., Kato, H., Nakakita, K., and Sudani, N., "80% Scaled NASA Common Research Model Wind Tunnel Test of JAXA at Relatively Low Reynolds Number," AIAA Paper 2013-0493, 51st AIAA Aerospace Sciences Meeting, 2013.

[5] Kohzai, M., Ueno, M., Koga, S., and Sudani, N., "Wall and Support Interference Corrections of NASA Common Research Model Wind Tunnel Tests in JAXA," AIAA Paper 2013-0963, 51st AIAA Aerospace Sciences Meeting, 2013.

[6] Murata, Y., Murayama, M., Kohzai, M., Yamamoto, K., Ura, H., Ito, Y., and Takaishi, T., "Aeroacoustic Testing of JAXA 8% Semispan High-Lift Common Research Model (CRM-HL) with Low-Noise Concepts," AIAA Paper 2026-3427, 32nd AIAA/CEAS Aeroacoustics Conference, 2026.

[7] Murata, Y., Murayama, M., Kohzai, M., Yamamoto, K., Ura, H., Ito, Y., Takaishi, T., Choudhari, M., and Lockard, D., "Model-Configuration Effects in Aeroacoustic Testing of the JAXA 8% CRM-HL," AIAA Paper 2026-3428, 32nd AIAA/CEAS Aeroacoustics Conference, 2026.

[8] Murayama, M., Yamamoto, K., Murata, Y., Kohzai, M., and Hirai, T., "CRM-HL Noise Prediction Based on LBM-VLES Compared with a Wind-Tunnel Test," Paper 2026-3426, 32nd AIAA/CEAS Aeroacoustics Conference, 2026.

[9] Ito, Y., Takaishi, T., Ozawa, Y., and Hirai, T., "Aeroacoustic Characteristics of Main Landing Gear of High-Lift Common Research Model," AIAA Paper 2025-3282, AIAA Aviation Forum, 2025.

[10] Ito, Y., Takaishi, T., Ozawa, Y., Kohzai, M., and Jawahar, H. K., "Main Landing Gear Noise Reduction Impact on JAXA 8% Semispan High-Lift Common Research Model," AIAA Paper 2026-3479, 32nd AIAA/CEAS Aeroacoustics Conference, 2026.

[11] Ozawa, Y., Ito, Y., Takaishi, T., Shimoda, K., Hirai, T., and Jawahar, H. K., "Effect of Noise-Reduction Devices on Wake Flow Behind Main Landing Gear of High-Lift Common Research Model," AIAA Paper 2026-3480, 32nd AIAA/CEAS Aeroacoustics Conference, 2026.

[12] Yokokawa, Y., Murayama, M., Uchida, H., and Tanaka, K., "Aerodynamic Influence of a Half-Span Model Installation for High-Lift Configuration Experiments," AIAA Paper 2010-684, 48th AIAA Aerospace Sciences Meeting, 2010.

[13] Hashioka, T., Murahashi, Y., Yasuda, H., Sawaki, Y., Onda, S., Tsuchimoto, Y., Nishizaki, Y., Suzuki, W., and Kawamura, T., "Test Summary of the Full-Span High-Lift Common Research Model at KHI Aeroacoustic Low-Speed Wind Tunnel," Proc. of the 34th ICAS Congress, 2024.

[14] Evans, A., Lacy, D., Smith, I., and Rivers, M., "Test Summary of the NASA Semi-Span High-Lift Common Research Model at the QinetiQ 5-Metre Low-Speed Wind Tunnel," AIAA Paper 2020-2770, June 2020. doi:10.2514/6.2020-2770.

[15] Lockard, D. P., Turner, T. L., Bahr, C. J., and Hutcheson, F. V., "Overview of Aeroacoustic Testing of the High-Lift Common Research Model," AIAA Paper 2021-2113, AIAA Aviation Forum, 2021.

[16] NASA Common Research Model – High-Lift CRM Geometry, https://commonresearchmodel.larc.nasa.gov/high-lift-crm/high-lift-crm-geometry/reference-geometry/

[17] Ertsgaard, M. L., and Winski, C. S., "Development of NASA 5.2% Semispan High-Lift Common Research Model (CRM-HL)," AIAA Paper 2025-1127, AIAA Scitech Forum, 2025.

[18] Eder, S., Hufnagel, K., and Tropea, C., "Semi-Span Testing in Wind Tunnels," Proc. of the 25th ICAS Congress, 2006.

[19] Uchiyama, T., Kohzai, M., Miki, H., Hirotani, T., Sudani, N., and Shutoku, H., "Experimental Investigation of a 160% Scaled NASA Common Research Model at Low-Speed Conditions," AIAA Paper 2019-2190, AIAA Scitech Forum, 2019.